Luminogens with Aggregation-Induced Emission

Luminogens with aggregation-induced emission (AIEgens) have been widely applied in the field of photodynamic therapy. Among them, aggregation-induced emission photosensitizers (AIE–PSs) are demonstrated with high capability in fluorescence and photoacoustic bimodal imaging, as well as in fluorescence imaging-guided photodynamic therapy. They not only improve diagnosis accuracy but also provide an efficient theranostic platform to accelerate preclinical translation as well.

1. Introduction

Although important advances in cancer diagnosis and therapy have been achieved over recent decades, cancer patients are still suffering from severe side effects and constant relapses [1][2]. Fortunately, photodynamic therapy (PDT) has been investigated as a noninvasive modality for cancer treatment owing to its high selectivity and low side effects since the end of 20th century [3][4]. A PDT system is usually composed of three separately nontoxic parts: a photosensitizing drug or photosensitizer (PS), a light source that emits visible and/or near-infrared (NIR) photons and molecular oxygen dissolved in the target tissue [5], and among them, PSs can transfer photon energy to surrounding oxygen molecules to produce reactive oxygen species (ROS); in particular, singlet oxygen ($^1O_2$) that causes cell death [6] is the most important one.

Porphyrins and phthalocyanines are the most widely studied PSs with fast intersystem crossing and long triplet lifetime and have already been applied in clinical applications [7][8]. Nevertheless, these PSs usually aggregate in aqueous media due to their low water solubility. This leads to low fluorescent intensity and PDT efficiency owing to the aggregation-caused quenching (ACQ) effect (Figure 1), which makes image-guided PDT difficult to achieve [9][10][11]. To solve this problem, some water-soluble and nonaggregating PSs have been synthesized [12]. However, such an approach greatly increased the cost of material preparation [13]. So, it is of great importance and is meaningful to develop novel PSs with outstanding fluorescent property in aqueous environments.
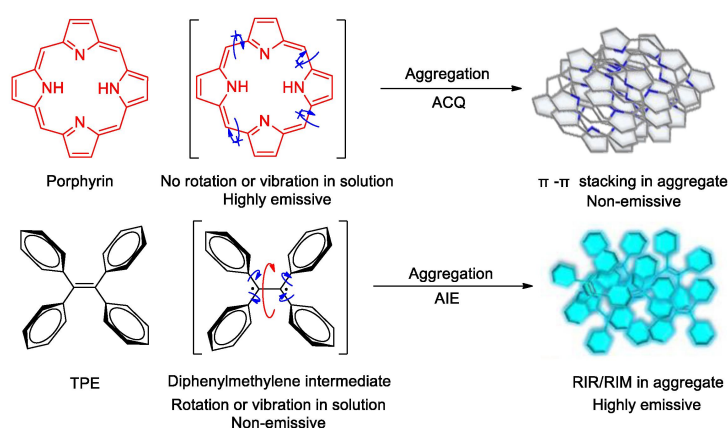

Figure 1. Schematic diagrams illustrating fluorescence quenching of traditional photosensitizers (PSs) such as porphyrin in their aggregate states vs. fluorescence turn-on effect of aggregation-induced emission (AIE) fluorogens such as tetraphenylethene (TPE) upon aggregate formation. Adapted and modified with permission from reference 15 (copyright 2015, American Chemical Society).

In 2001, a new concept termed as aggregation-induced emission (AIE) was proposed by Tang and co-workers [14][15], and since then, a series of luminogens with aggregation-induced emission property (AIEgens) have been developed. A typical AIEgen shows neglectable emission in dilute solutions but much enhanced emission in molecular ensembles [16][17]. In other words, AIEgens can utilize aggregation to play a positive instead of a negative role in enhancing luminescence [18]. The systematic study of the mechanism has profoundly revealed the molecular mechanism of the AIE phenomenon:

molecules with AIE characteristics often have a propeller-like configuration—a number of conjugated units are connected through single bonds that can rotate [19]. In dilute solutions, the conjugated units within the molecule can rotate upon the promotion of solvent molecules. When molecules are excited by light or other energy sources, these rotations consume almost all of the excited state energy (non-radiation decay, e.g., thermal motion), and the molecules emit very weak luminescence or are even non-emissive. When the molecules aggregated, the conjugated units can be bound by the enhanced intermolecular interactions, and their rotations are evidently inhibited. Thus, the channels for non-radiation decay are largely closed and the excited state energy of the molecules is released in the form of fluorescence/phosphorescence (radiation decay). As a result, luminescence can be observed. This mechanism for AIE phenomenon is termed as restricted intramolecular rotation (RIR) [19][20][21][22]. On the other hand, AIE properties have been observed for some conjugated molecules with shell or butterfly wing-like structures [23][24]. The results of systematic study indicate that their AIE behavior is due to the molecular vibration. The opening/closing of the shells or the flapping of the butterfly wings of these kinds of molecules consume their excited state energy, causing them with lack emission in dilute solution, while they are strongly emissive in the aggregated state as the intramolecular vibrations are restricted. This is another mechanism of AIE phenomenon explained as restricted intramolecular vibration (RIV) [25]. Nowadays, the RIR and RIV mechanisms are integrated into the restricted intramolecular motions (RIM) theory for AIE phenomenon [15].

AIEgens with free rotational/vibrational structures can enhance the intersystem crossing (ISC) between the excited singlet state (S_1) and the excited triplet state (T_1), and thereby increase the quantum yield and lifetime of the triplet state, as well as the efficiency of ROS generation. Taking advantage of the high-efficiency luminescence in an aggregated state, nanoparticles prepared from AIE molecules (AIE–dots) can exhibit strong luminescence as well as good photostability in the bio-system, and effectively overcome the shortcomings of the traditional dye with ACQ property. Therefore, aggregation-induced emission photosensitizers (AIE–PSs) can present huge potential in the field of imaging-guided PDT [26][27].

2. Aggregation-Induced ROS Generation Mechanism

Absorption of a photon leads to the formation of an "excited state" of the photosensitizing agent. As illustrated in Figure 2, the common features of the electronic excitation and the consequent photochemical reactions may be described by three electronic states: singlet ground state (S_0), singlet excited states (S_1, S_2), and longer-lived triplet excited state (T_1).
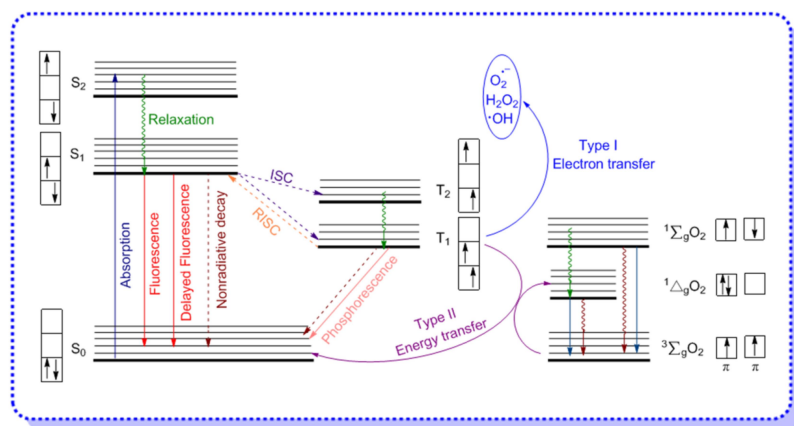

Figure 2. Photophysical and photochemical processes illustrated by a modified Jablonski energy diagram: The aggregated aggregation-induced emission photosensitizer (AIE–PS) in singlet excited (S_1) state may undergo intersystem crossing (ISC) to an excited triplet state (T_1) and then generate reactive oxygen species (ROS). Adapted and modified with permission from references 5 (copyright 2017, Elsevier), 6 (copyright 2016, Royal Society of Chemistry), and 16 (copyright 2020, Wiley-VCH).

Electronic absorption occurs between the vibrational and rotational energy levels of the excited singlet states. Immediately after photon absorption, several photophysical and photochemical processes occur, but the most likely deactivation pathway is a relaxation to the lowest vibrational energy level of the first excited state. This very fast process (10^{-15} s) is defined as relaxation. For AIE–PSs in the aggregated state, the non-radiative decay process such as intramolecular rotation (RIR) and intramolecular vibration (RIV) will be restricted in the excited state. If relaxation from S_1 is accompanied by emission of a photon, the process is known as fluorescence. Several other relaxation pathways compete with the photonic processes are also described above, and among them, the most important one is a nonradiative process to the lowest excited triplet state (T_1), which is known as intersystem crossing (ISC). The latter event may result in either the emission of a photon from triplet excited state (T_1) through spin-forbidden phosphorescence, or the photochemical reactions. It is noteworthy that molecules in the excited states are generally stronger oxidizing and reducing species than

their analogues in the ground states. Thus, apart from the radiative decay processes of fluorescence and phosphorescence, the exciton may also undergo internal conversion to release energy as heat, or generate ROS by the electron transfer (Type I)/energy transfer (Type II) of triplet oxygen [28][29].

Before introducing the mechanism of electron transfer and energy transfer while generating ROS, we need to understand the electronic structure of singlet oxygen and triplet oxygen first. As shown in Figure 2, molecular oxygen has two low-lying singlet excited states, the first excited state ($^1\Delta_g$) and the second excited state ($^1\Sigma_g$), which are 95 and 158 kJ mol^{-1} above the triplet state ($^3\Sigma_g$), respectively, and the only difference in their electronic configuration is the structure of the π-antibonding orbitals. For $^1\Delta_g$, the configuration of the molecular orbitals is: O_2 $[KK(\sigma_{2s})^2(\sigma^*_{2s})^2(\sigma_{2px})^2(\pi_{2p})^4(\pi^*_{2py})^2(\pi^*_{2pz})^0]$, while for $^1\Sigma_g$, the electronic configuration is identical to that of the ground state, except that the last two electrons have antiparallel spins. Normally, the transition from the $^1\Delta_g$ state to the $^3\Sigma_g$ state is spin forbidden, which means that the $^1\Delta_g O_2$ is a relatively long-lived species, meanwhile, the second excited state of oxygen is short-lived due to its spin-allowed transition to the $^1\Delta_g$ state, and all of these have been confirmed by the radiative lifetimes of O_2 ($^1\Delta_g$) and O_2 ($^3\Sigma_g$) [30].

2.1. Electron Transfer (Type I) Mechanism

As reported in the literature, molecules in the excited state always have larger oxidation/reduction potential than their ground state analogs [5]. AIE–PSs can generate superoxide anion ($O_2^{\bullet-}$), hydroxyl radical ($\bullet$OH), peroxide (O_2^{2-}), and other free radical ROS through electron transfer under low concentrated oxygen conditions. The first oxygen-centered radical generated according to Type I mechanism is $O_2^{\bullet-}$. It is formed when an electron is captured by one of the π^*_{2p} orbitals of oxygen either in the presence of a reducing agent or directly from an excited photosensitizer.

The reduction potential of superoxide ion may change with the surrounding environment. For example, $O_2^{\bullet-}$ is a weak oxidizing agent in aqueous media, but it is still able to oxidize to, for example, ascorbic acid [31]. Meanwhile, it can also act as a strong reducing agent and enable the reduction of iron complexes in cytochrome c, as well as in the ferric/ethylene diamine tetraacetic acid (EDTA) complex [32]. The subsequent perhydroxyl radical is formed. The perhydroxyl radical is a more potent oxidant than superoxide ion, thus it is able to oxidize $O_2^{\bullet-}$ and resulting in the H_2O_2 formation. Dismutation of $O_2^{\bullet-}$ is often occur under the catalysis of superoxide dismutase (SOD) or PS, and leads to the formation of hydrogen peroxide (H_2O_2), which is characterized by a much longer half-life than other kinds of ROS. In contrast with other kinds of ROS, H_2O_2 can pass through biological membranes and cause the damage of other cellular compartments [33]. Moreover, H_2O_2 can be detoxified by the enzyme catalase, resulting in the formation of water and molecular oxygen, or may further react with either superoxide ion, or form highly reactive hydroxyl radicals. The produced hydroxyl radicals are able to oxidize major biologically relevant molecules such as proteins, lipids, carbohydrates, and DNA, and are also able to inactivate natural antioxidants (e.g., tocopherol).

In view of the possible electron transfer from the PS in triplet excited state, the mechanism of hydroxyl radical generation through photocatalysis is proposed and presented in Figure 3. Although H_2O_2 is a worse electron acceptor than molecular oxygen, electron transfer reaction from PS* to H_2O_2 may occur if the PS triplet state lifetime is long enough [34]. Under the biological conditions with ferrous ions, H_2O_2 can undergo the Fenton reaction and produce hydroxyl radicals by one-electron reduction, meanwhile, the produced ferric iron can be reduced back to the ferrous state by superoxide for further use, which is termed the iron-catalyzed Haber–Weiss reaction [35]. On the other hand, H_2O_2 can react with the sensitizer radical anion to form hydroxyl radicals and hydroxide anion. The results of the completed and ongoing projects show that PDT is more effective if mechanism I is operative and completed with the generation of highly reactive hydroxyl radicals [36][37][38].
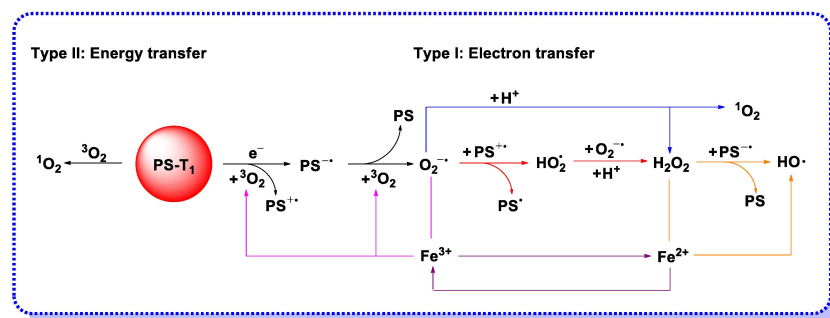

Figure 3. ROS generation mechanism: Type I electron transfer to form free radical ROS and hydrogen peroxide, and Type II energy transfer to form singlet oxygen.

2.2. Energy Transfer (Type II) Mechanism

Based on the characteristics of singlet/triplet oxygen electrons and energy levels, the Type II mechanism means the energy transfer from the triplet excited state of an AIE–PS to the ground state of molecular oxygen. Most of the PDT agents produce singlet oxygen ($^1O_2$, $^1\Delta_g$) via a Type II mechanism, which can oxidize the nearby biological species and lead to cytotoxicity. The unoccupied π^*_{2p} orbital of these singlet oxygen makes it highly reactive toward electron-rich compounds. For example, $^1O_2$ can oxidize lipids to produce hydroperoxides, and also can react with amino acids (such as tryptophan, tyrosine, histidine, methionine, cysteine, and cystine) to form hydroperoxides and endoperoxides, which are also the products of oxidation reaction between $^1O_2$ and deoxyguanosine presented in DNA. The above reactions are subsequently responsible for cellular toxicity, but the cytotoxic effects induced by $^1O_2$ are independent of the activity of the antioxidant enzymes.

The triplet energies for many AIEgens exceed the energy requirement of the generation of $^1O_2$ ($^1\Delta g$), which is reported as 22.5 kcal/mol [39][40]. Hence, most AIE–PSs can generate singlet oxygen efficiently [41][42], and the most common mechanism for generating $^1O_2$ is the quenching process of the PS excited states with molecular oxygen.

3. AIE–PSs Based on Electron Transfer (Type I) Mechanism

Similar to the development of ACQ–PSs, few reports were available on the capability for Type I ROS generation of AIE–PSs [43]. In 2020, Tang and Zhao reported two new Type I PSs, α-TPA-PIO and β-TPA-PIO, from phosphindole oxide-based isomers with efficient Type I ROS generation abilities (Figure 4) [44]. The AIE attributes of α-TPA-PIO and β-TPA-PIO were investigated in DMSO/water mixtures, by employing water as a poor solvent. The emission intensity of β-TPA-PIO in pure DMSO solution was very weak. By increasing the fraction of the water, the emission intensity increased gradually and boosted up quickly when the water fraction was over 80%. The emission intensity of the mixture with 99% H_2O was about 90 times higher than in pure DMSO (λ_{em} = 560 nm). The AIE property of α-TPA-PIO was similar to β-TPA-PIO. These results indicated that α-TPA-PIO and β-TPA-PIO were typical AIEgens. To validate the ROS generation ability, electron paramagnetic resonance (EPR) spectroscopy using 5-tert-butoxycarbonyl-5-methyl-1-pyrroline-N-oxide (BMPO) as a spin-trap agent was carried out to monitor the formation of oxygenous radicals. EPR showed the typical EPR spectra of oxygenous radical adducts formed with BMPO after white light irradiation of 100 mW cm^{-2} for 5 min, which was in good agreement with those in the literature. α-TPA-PIO, β-TPA-PIO and crystal violet (CV) exhibited similar BSA-promoted signal enhancements, but β-TPA-PIO exhibited the strongest EPR signal intensity, indicative of its best generation ability of oxygenous radicals, namely Type I ROS. These two PSs could be selectively accumulated in a neutral lipid region, particularly in the endoplasmic reticulum (ER) of cells and efficiently induce ER-stress mediated apoptosis and autophagy in PDT. In vivo models indicated that β-TPA-PIO successfully achieved remarkable tumor ablation. The ROS-based ER stress triggered by β-TPA-PIO-mediated PDT had high potential as a precursor of the immunostimulatory effect for immunotherapy.
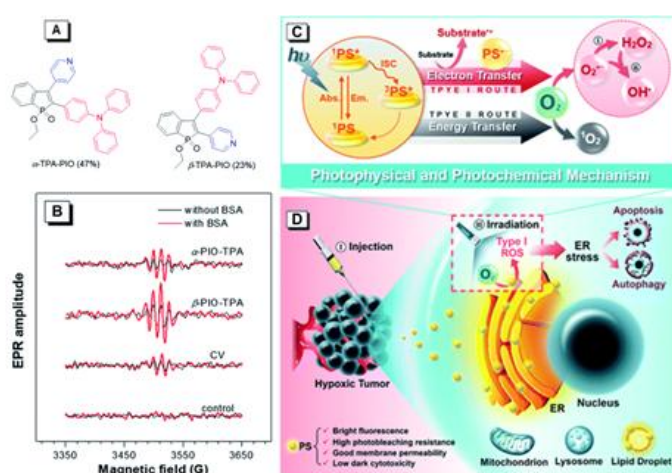

Figure 4. (**A**) Chemical structures of α-TPA-PIO and β-TPA-PIO. (**B**) Electron paramagnetic resonance (EPR) signals of BMPO (for Type I ROS detection) in the presence of 1 mM α-TPA-PIO, β-TPA-PIO or CV (without/with 500 nM BSA) in PBS with 1 vol % DMSO. Schematic illustration of (**C**) photophysical and photochemical mechanisms and (**D**) the cytological process of photodynamic therapy (PDT) treatment mediated by phosphindole oxide based fluorogens. (i) Disproportionation reaction; (ii) Haber–Weiss/Fenton reaction. Adapted and modified with permission from reference 44 (open access 2020, Royal Society of Chemistry).

4. AIE-PSs Based on Energy Transfer (Type II) Mechanism

As the energy transfer process is faster than the electron transfer process, most of the PSs reported so far for AIEgens are singlet oxygen ROS generators. There are several ways to distinguish Type II mechanism from a Type I one. For example, direct monitoring $^1O_2$ formation involves the detection of its phosphorescence at 1270 nm. Actually, the use of a variety of specific fluorescent probes is the most common way to detect the singlet oxygen generated by AIE–PSs. The following is a summary of the Type II AIE–PSs applied in the design of new ROS generation system for PDT in recent years.

As reported in the literature, the smaller the singlet–triplet energy gap (ΔE_{ST}), the higher the ISC rate, and designing molecules with a D-A structure is one of the most effective way to reduce the ΔE_{ST} [45]. In order to illustrate energy transfer in AIE–PSs clearly, the structure of AIE cores are divided into three categories: "neutral" AIE core, "donor" AIE core and "acceptor" AIE core, the latter two are based on the electron withdrawing/donating abilities of the core structures (Figure 5) [46][47][48]. Based on this, AIE–PSs of Type II can be divided into two categories: donor-AIE (neutral)-acceptor and AIE (donor)-acceptor. The photophysical properties, photosensitivity efficiency and singlet oxygen quantum yield of all the AIE–PSs are shown in Table 1.
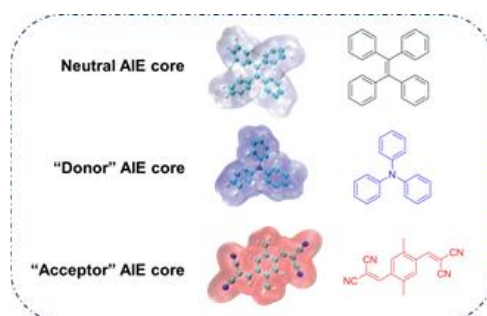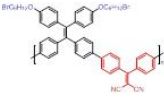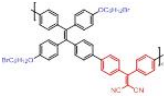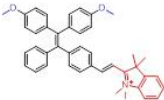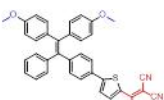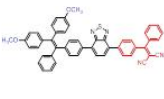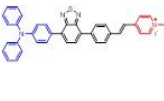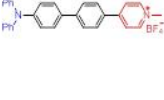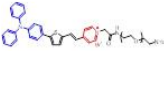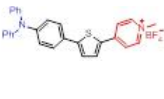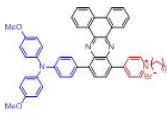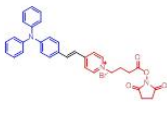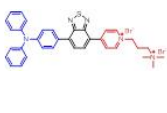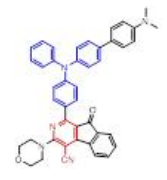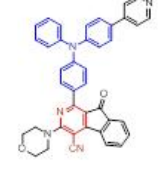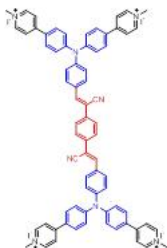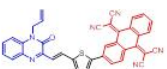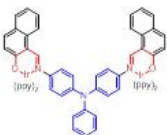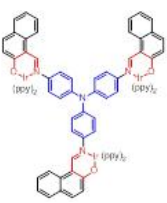

Figure 5. Classification of neutral, donor and acceptor AIE cores by their electron characters, the electronic clouds are represented by colored clouds (the neutral, donor and acceptor AIE cores are represented by the black, blue and red scheme, respectively).

Table 1. Chemical structures, absorption/emission peaks, ΔE_{ST}, consuming rate of ABDA, treatment efficiency and singlet oxygen quantum yield of different AIE–PSs (the donor and acceptor groups of different AIE–PSs are represented by the blue and red scheme, respectively).

AIE-PSs	Chemical Structures	Absorption/Emission [nm]	ΔE_{ST} [eV] [a]	Consuming Rate of ABDA	Treatment Efficiency	$^1O_2$ Quantum Yield [b]	Ref.
		Donor-AIE (Neutral)-Acceptor AIE–PSs					
1		520/820	0.067	3.58 nmol min^{-1}	IC$_{50}$ = 5.0 µg mL^{-1} (4T1 cell) White light: 60 mW cm^{-2} for 5 min	0.08	[49]
2		410/620	0.23	3.98 nmol min^{-1}	IC$_{50}$ = 8.0 µg mL^{-1} (4T1 cell) White light: 60 mW cm^{-2} for 5 min	-	[50]
3		440/606	-	-	IC$_{50}$ = 1.5 × 10^{-6} M (HeLa cell) White light: 36 mW cm^{-2} for 40 min	-	[51]

#	Structure	λ (nm)					Ref.
4		410/610	-	9.03 nmol min^{-1}	-	-	[50]
5		410/620	-	21.8 nmol min^{-1}	-	0.55	[50]
6		480/710	0.63	-	IC$_{50}$ = 70.72 µg mL^{-1} polymer (HeLa cell) White light: 100 mW cm^{-2} for 5 min	0.89	[52]
7		450/651	0.50	12.0 nmol min^{-1}	-	-	[45]
8		450/650	0.33	27.0 nmol min^{-1}	IC$_{50}$ = 1 µg mL^{-1} (MDA-MB-231) White light: 60 mW cm^{-2} for 5 min	Higher than 0.08	[53]
				AIE (Donor)-Acceptor AIE–PSs			
9		447/625	0.15	-	-	-	[54]
10		442/558	-	70.20 nmol min^{-1}	55% killing effect of HeLa cell 10 × 10^{-6} M White light: 60 mW cm^{-2} for 30 min	3.17	[55]
11		480/680	-	-	IC$_{50}$ = 10.0 µg mL^{-1} (4T1 cell) White light: 24 mW cm^{-2} for 30 min	-	[56]
12		448/592	-	121.74 nmol min^{-1}	75% killing effect of HeLa cell 10 × 10^{-6} M White light: 60 mW cm^{-2} for 30 min	3.71	[55]

No.	Structure	λ (abs/em)			Activity		Ref.
13		508/720	0.093	-	83.2% killing effect of *E. Coli* 10 × 10⁻⁶ M White light: 60 mW cm⁻² for 10 min	0.71	[42]
14		457/630	-	-	79% killing effect of *P. aeruginosa* 10 × 10⁻⁶ M White light: 4.2 mW cm⁻² for 30 min	0.72	[57]
15		486/705	0.79	18.2 nmol min⁻¹	98.4% killing effect of *E. Coli* 10 × 10⁻⁶ M White light: 4.2 mW cm⁻² for 30 min	-	[58]
16		493/685	-	15.3 nmol min⁻¹	87.3% killing effect of *E. Coli* 10 × 10⁻⁶ M White light: 4.2 mW cm⁻² for 30 min	-	[58]
17		469/652	-	-	IC_{50} = 1.1 × 10⁻⁵ M (HeLa cell) White light: 20 mW cm⁻² for 30 min	-	[59]
18		417/601	0.09	-	-	-	[13]
19		409/593	0.16	0.7 nmol min⁻¹	-	-	[13]
20		405/580	-	-	IC_{50} = 3.0 × 10⁻⁷ M (HeLa cell) White light: 4 mW cm⁻² for 10 min	0.98	[60]

21		440/590	0.55	-	More than 70% killing effect of *E. Coli* 5×10^{-6} M White light: 10 mW cm^{-2} for 15 min	0.98	[61]
22		530/800	0.12	-	IC$_{50}$ = 3.26 µg mL^{-1} (Hela cell) White light: 100 mW cm^{-2} for 5 min	0.63	[62]
23		469/671	-	-	IC$_{50}$ = 6.3×10^{-6} M (HeLa cell) White light: 20 mW cm^{-2} for 30 min	-	[59]
24		469/690	-	-	IC$_{50}$ = 1.1×10^{-6} M (HeLa cell) White light: 20 mW cm^{-2} for 30 min	-	[59]

[a] The data of singlet-triplet energy gap were theoretical calculation results according to references; [b] quantum yield was estimated in reference to Rose Bengal.

4.1. Donor-AIE (Neutral)-Acceptor PSs

Table 1 shows the donor-AIE (Neutral)-acceptor PSs that have been reported in recent years [49][50][51][52][53][63]. AIE–PSs **1**–**8** all possess an electron donor and an acceptor on a tetraphenylethene (TPE)-conjugated skeleton, and can induce the effective generation of reactive oxygen species (ROS) for PDT. High $^1O_2$ generation efficiency can be obtained through inorganic–organic hybridization, chemical linkage, etc. Among them, AIE–PSs **1**–**6** are all constructed in the way of D-π-A, while AIE–PSs **7** and **8** use thiophene and benzothiazole to extend the conjugated structure in the D-π-A structure, which can decrease ΔE_{ST} effectively. The characteristics of several typical PSs of this type are described as follows, for example, **NP-1** was prepared via the encapsulate of AIE–PS **1** by encapsulation of AIE–PS **1** using surfactant (DSPE-PEG-MAL) as the polymer matrix, and then followed by the surface decoration of HIV-1 transactivator (RKKRRQRRRC) (Figure 6A) [49]. It could emit near-infrared (NIR) fluorescence centered at 820 nm, and displayed $^1O_2$ generation ability even greater than that of Ce6, one of the most efficient PSs reported so far [64][65]. Similarly, Liu and co-workers designed and synthesized two conjugated polymer PSs of **4** and **5** based on a small molecule AIE–PS **2** [50]. Subsequently, they were encapsulated by an amphiphilic polymer to yield nanoparticles for both in vitro cancer cell ablation and in vivo zebrafish liver tumor treatment via two-photon excited photodynamic therapy (2PE-PDT) with high efficiency. Under two-photon excitation, **4** and **5** showed high efficiency of $^1O_2$ production in aqueous solutions and cells due to the enhanced ISC process and molecular conjugation, and among them, **5** presented higher $^1O_2$ generation efficiency compared with **2**. This two-photon photodynamic therapy could perform precise 3D manipulation of the treatment volume, and provide a target level that cannot be achieved with current treatment technology.
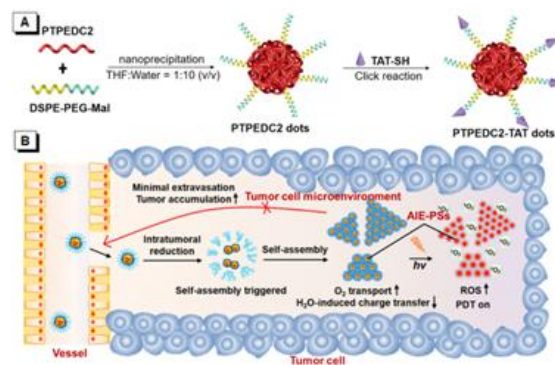
Figure 6. (**A**) Schematic illustration for the synthesis of AIE–PS dots and Aggregation-induced emission trans-activating protein (AIE-TAT) PS dots using PTPEDC2 as an example. Adapted and modified with permission from reference 50 (copyright 2019, American Chemical Society). (**B**) Schematic illustration of in vivo self-assembly of nanoparticle **8**. Adapted and modified with permission from reference 53 (copyright 2020, American Chemical Society).

In recent years, many AIE–PS nanoparticles (NP) have been designed based on the same strategy [52][53]. Moreover, by connecting thiophene ring or benzothiophene ring between the donor and the acceptor structure, AIE–PS with red-shifted emission and better performance can be obtained [66][67]. Wang reported a metal–organic framework (ZIF-8, ZIF = zeolitic imidazolate framework) by AIE–PS **8** assisted in vivo self-assembly nanoplatform, ZIF-8-PMMA-S-S-mPEG (nanoparticle **8**), as an effective tool for organic PS payload to achieve efficient PDT [53]. As shown in Figure 6B, when nanoparticle **8** went through the vessel and entered the tumor tissue owing to the suitable size (about 50 nm), the mPEG chain would cleave under the effect of the disulfide bonds in the tumor, trigger the self-assembly of PS@ZIF-8-PMMA with the AIE-NPs nearby, and promote the retention of AIE–PSs in the tumor significantly because of their relatively large size of 200 nm. When O_2 was delivered to AIE–PSs, $^1O_2$ could be produced and maintain in the tumor for a long time. This strategy achieved the largest intratumoral $^1O_2$ photosensitization of organic PS loaded with organic PS under light activation. It was proved to be advantageous for organic PSs typically suffering from moderate tumor accumulation and compromised intratumoral ROS generation.

4.2. AIE (Donor)-Acceptor PSs

Another kind of most widely used core for the preparation of AIE–PSs is triphenylamine and its analogues. Triphenylamine is not only the core of AIE–PSs but also a typical electron donor, so this type of photosensitizers is called "AIE (Donor)-Acceptor PSs". As reported, triphenylamine moiety has been widely used to enhance the AIE effect of the PSs and pyridinium group is proved to be a specific targeting site toward mitochondria [55][68][69]. The two kinds of moiety are bridged through different units such as phenyl and thiophene groups to regulate the molecular electron effect. As shown in Table 1 (AIE–PSs **9**–**19**), most of the AIE (donor)-acceptor AIE–PSs are constructed in this way and exhibit good performance [42][56][58][59]. For instance, **10** and **12**, respectively, showed strong AIE with the emission enhancement up to 290-fold and 34-fold, large two-photon absorption cross-section up to 477 and 303 GM, respectively, and highly specific targeting to mitochondria in living cells with good biocompatibility [55]. When **10** and **12** were excited at 405 nm, they could emit a light peak at about 800 nm, and produce ROS as well. Therefore, they showed great potential in the clinical application of cell/tissue bioimaging by two-photon fluorescence as well as the image-oriented and mitochondrial photodynamic cancer therapy.

Besides, Tang et al. proposed a new strategy for imaging and killing certain bacteria at the same time, which was suggested to form a new class of antibacterial conjugated organisms (TVP-PAP) by integrating AIEgens together with bacteriophages (Figure 7). AIE molecule **14** displayed excellent fluorescent characteristics, effective PDI activity and it could be easily modified to the surface of phage entities through a simple amino-carboxyl reaction. The generated TVP-PAP perfectly retained the characteristics of the AIEgen and bacteriophages, and entrusted the inherent AIE fluorescence with both the function of real-time monitoring and bacterial targeting. Moreover, by significantly exceeding two individuals in the bioconjugate, it was endowed with an effective synergistic antibacterial effect [57]. The in vitro test demonstrated that even MDR *P. aeruginosa* could be nearly 100% killed, attributed to the synergistic effect within TVP-PAP.
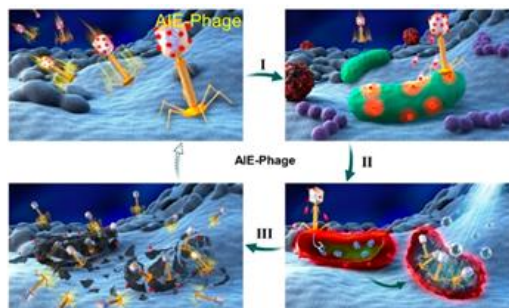
Figure 7. Phage-guided targeting, discriminative imaging, and synergistic killing of bacteria by AIE bioconjugates. The processes are as follows: (**I**) the particular recognition of bacteria by AIEgen conjugated phage; (**II**) the bacterial lighting up imaging by AIE fluorescence and the phage infections as well as the ROS generation of luminogens with aggregation-induced emission (AIEgens); (**III**) the synergistic killing of the target bacteria by phage infections and AIE-based photodynamic inactivation. Adapted and modified with permission from reference 57 (copyright 2020, American Chemical Society).

Moreover, to improve the efficiency of ROS generation, Tang and his co-workers adopted the method of supplying more donor/acceptor electronic cores to construct AIE–PSs [60][61]. As a representative, AIE–PS **20** possessed an ultra-high $^1O_2$ quantum yield of 98.6% in water; the PS of **20** could efficiently induce cell death in a series of carcinoma cells (IC_{50} values less than 300×10^{-9} M) upon irradiation with an extremely low fluence (460 nm, 4 mW cm^{-2} for 10 min) [60]. Atypical structures such as AIE–PS **22** were also classified into this category as they containing -CN groups with electrons that are strongly attractive. Compared with the part that strongly attracts electrons, the other part can be regarded as "donor" core. Photosensitizer **22** showed strong NIR emission centered at 800 nm, good photostability, and high $^1O_2$ generation efficiency and could induce more tumor cell apoptosis than traditional PSs (CE6) [62]. In addition, Xie et al. rationally designed red-emitting AIE Ir(III) complexes **23** and **24** with different central metal numbers (di-nuclear and tri-nuclear) in 2019. It provided the possibility to develop multi-nuclear Ir(III) complexes with long excitation wavelength for in vivo imaging and PDT [59].

Connecting TPE to the atypical AIE (donor)-acceptor structure is also a typical method to construct the near-infrared AIE–PSs. For example, Tang and his team used amphiphilic polymers (i.e., DSPE-PEG2000 and DSPE-PEG2000-MAL) to encapsulate the hydrophobic upconversion nanoparticles (UCNPs) and AIE–PSs **25** (Figure 8) [70]. With high photostability, the prepared UCNP@**25**-cRGD NPs could maintain their fluorescent intensity above 70% after 30 days, and under NIR light illumination, a significant amount of ROS could still be detected even when covered within a 6 mm tissue. The UCNP@**25**-CRGD NPs could specifically target $\alpha_v\beta_3$ integrin over-expressed MDA-MB-231 cells and selectively kill these cells in both 2D and 3D cancer models upon NIR light illumination, without obvious dark cytotoxicity. The results of in vivo antitumor evaluation demonstrated that with NIR light illumination, the intravenously injected UCNP@**25**-cRGD NPs could light up the tumors and significantly induce apoptosis of tumor cells, and thus inhibit the growth of large tumors in a mouse model compared to white light illumination.
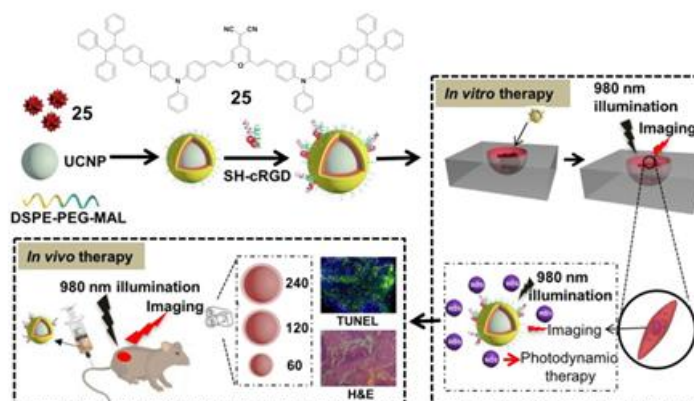
Figure 8. A rational design for a near-infrared (NIR) light-regulated theranostic nanoplatform based on AIE luminogen-encapsulated upconversion nanoparticles. Schematic illustration of preparation of UCNP@**25**-cRGD nanoparticles and their applications in bioimaging and PDT of deep-seated tumors upon NIR laser illumination, in an in vitro three-dimensional (3D) cancer cell spheroid and in a murine tumor model, respectively. Adapted and modified with permission from reference 70 (open access 2019, Theranostics).

5. Both Energy Transfer and Electron Transfer AIE–PSs

As mentioned above, ROS mainly includes two types, among which superoxide anion ($O_2^{\bullet-}$), hydroxyl radical (•OH), peroxide (O_2^{2-}), and so on fall into Type I, while singlet oxygen ($^1O_2$) belongs to Type II. However, there exist some AIE–PSs that can react with oxygen to form both $O_2^{\bullet-}$/•OH/O_2^{2-} and $^1O_2$. For example, AIE –PSs **18** and **19** mentioned in Section 4.2 are mainly PSs of Type II, but their protonated products, **26** and **27** NPs are quite different (Figure 9) [13]. Through research, it is found that the ROS and $^1O_2$ generation capacity of **19** and **27** NPs are inconsistent. Tang suggested that **27** produces not only $^1O_2$ but also ROS. To explain this observation, sodium azide (NaN₃) as a $^1O_2$ quencher was added to the 9, 10-anthracenediylbis (methylene)dimalonic acid (ABDA) solution in the presence of **19**, **26**, or **27** NPs. Gradually, the absorption of ABDA with **26**, or **27** declined with prolonged irradiation time even at a high concentration of NaN₃ (240 mg/mL). In addition, dihydroethidium (DHE) was used as a sensitive $O_2^{\bullet-}$ probe to assess the $O_2^{\bullet-}$ generation in HeLa cells by flow cytometry. Results showed that the fluorescence of HeLa cells with DHE became stronger in the presence of **26**, or **27** under light irradiation. Clearly, **26** and **27** could generate a small amount of $O_2^{\bullet-}$, which is the precursor of •OH and H_2O_2. Tang also used the indicator to detect the type of active oxygen. AIE–PS **28** exhibited a prominent AIE property with strong NIR fluorescence in aggregates and was capable of efficiently generating ROS of $O_2^{\bullet-}$ and $^1O_2$ under white light irradiation (Figure 10) [71]. To demonstrate the AIE property of **28**, its emission behavior in THF/water mixtures with different volume fractions of water (f_w, vol %) was examined. The results showed that the emission peak of **28** moved to 690 nm and intensified greatly in the mixture with f_w of 90, indicating a prominent AIE characteristic. This type of NIR photosensitizer with AIE characteristic could be a promising alternative for the fabrication of nanoprobes and nanomedicines for the potential clinical applications of multiple tumors.
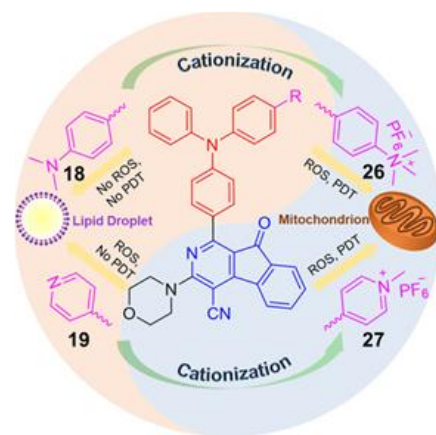
Figure 9. Chemical structures of AIE–PSs **18**, **19, 26,** and **27** (among them, **18** and **19** have low ROS generation efficiency, and **26** and **27** with cations can have high ROS generation efficiency). Adapted and modified with permission from reference 13 (copyright 2019, American Chemical Society).
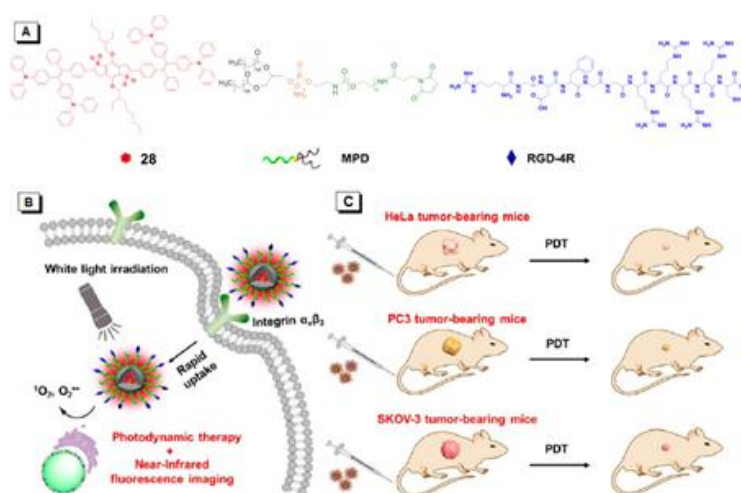
Figure 10. (**A**) Chemical structures of AIE–PS **28**, 1,2-distearoyl-*sn*-glycero-3-phosphoethanolamine -*N*-[maleimide(polyethylene glycol)-2000] (MPD), and RGD-4R. (**B**) Cellular uptake and PDT process of RGD-4R-MPD/**28** NPs. (**C**) Xenograft tumor models of cervical, prostate, and ovarian cancers are established with HeLa, PC3, and SKOV-3 cells, respectively. Adapted and modified with permission from reference 71 (copyright 2020, American Chemical Society).

In addition to the usage of indicators to detect the type of ROS, the operation of instruments is also completely feasible. As shown in Figure 11A, EPR spectroscopy was used to provide solid evidence for the free radical ROS generation of four AIE–PSs [54]. Both BMPO under irradiation and BMPO + AIEgens (**30** and **31**) in the dark did not produce any signal

in the EPR spectra. In contrast, significant EPR signals could be observed upon irradiation of the BMPO + **30/31** solution, associated with the production of paramagnetic free radical species. Thus, it could be confirmed that **9** with low intramolecular charge transfer (ICT) produced only $^1O_2$, species. According to the results derived from **29** and naphtho[2,3-c][1,2,5]thiadiazole-based (NZ-based) AIE–PSs, once the ICT intensity was enhanced by a donor with strengthened electron-releasing ability (Figure 11B), the $^1O_2$, species were transformed into free radical ROS, which agreed well with the proposal of "more ICT leading to the generation of more free radical ROS".

Figure 11. (**A**) EPR signals of BMPO for free radical ROS characterization. Adapted and modified with permission from r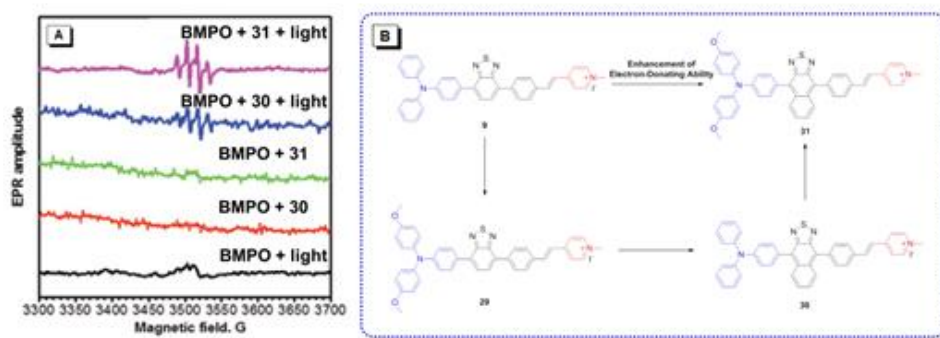eference 54 (copyright 2020, Wiley-VCH). (**B**) Chemical structures of AIE–PSs **9**, **29**–**31** (the donor and acceptor groups are represented by the blue and red scheme, respectively).

6. Conclusions and Outlooks

As a noninvasive treatment, PDT has been extensively studied for both cancer diagnosis and therapy. Notably, the therapeutic effect of PDT is directly influenced by the ROS-generation ability of PSs. The emerging AIE–PSs and their application for image-guided therapy have shown evident advantages over the classical ones and thus have attracted much attention recently. In recent reports, the classification of the Type I and Type II AIE–PSs oxidation reactions is still not clearly categorized. Thus, in this brief review, we have tried to classify the AIE–PSs according to the following standards: (1) Type I: AIE–PSs generates superoxide anion ($O_2^{\bullet-}$), hydroxyl radical (•OH), peroxide (O_2^{2-}), and other free radical ROS through electron transfer. Electron transfer can actually occur in either direction, but most commonly, the excited sensitizer acts as an oxidant. Therefore, this type of AIE–PSs can achieve the purpose of PDT under hypoxic conditions. (2) Type II: AIE–PSs generate singlet oxygen ($^1O_2$) through energy transfer. This process must be under the condition of concentrated oxygen to convert triplet oxygen into singlet oxygen. (3) Type I and Type II: AIE–PSs generate both free radical ROS and $^1O_2$ through electron transfer and energy transfer, respectively. In the case of Type II, electron transfer occurs from the AIE–PSs to oxygen, and the generation of oxidation sensitizer and $O_2^{\bullet-}$ is also assigned to this category. Simultaneously, we classify the Type II PSs into two categories: donor-AIE (neutral)-acceptor and AIE (donor)-acceptor. The construction principle is to form a D-A and/or a D-π-A structure.

The reported that AIE–PSs have rendered new power to PDT, however, it could be noticed that most of the AIE–PSs used in PDT nowadays are Type II PSs. In fact, the development of Type II PSs will be seriously influenced by the fundamental paradox which existed between the high O_2 dependency of AIE–PSs and the hypoxic (not anaerobic) nature around solid tumors caused by insufficient blood supply. Furthermore, during the PDT process, especially in the continuous treatment, the photochemical consumption of O_2 as well as the micro-vascular damage will aggravate the O_2 shortage, and restrict the effect of PDT to an unsatisfactory outcome. An effective pathway to solve this problem is to design new PSs with low requirement of O_2 and can adapt to the hypoxic environment around the tumor tissues. Compared to the Type II PSs, Type I PSs with stronger hypoxia tolerance are a good choice, so the subsequent development of Type I AIE–PSs is full of opportunities and challenges in the future. In addition, methods for distinguishing two different mechanism types of ROS generation are also imperative to provide an insight into the ROS formation mechanism of AIE–PSs. If only considering the effect of medical treatment, the development of two-photon AIE–PSs with high reactive oxygen generation efficiency is also crucial.

References

1. Zou, J.; Lu, H.; Zhao, X.; Li, W.; Guan, Y.; Zheng, Y.; Zhang, L.; Gao, H. A multi-functional fluorescent probe with aggregation-induced emission characteristics: Mitochondrial imaging, photodynamic therapy and visualizing therapeutic process in zebrafish model. Dyes Pigm., 2018, 151, 45–53.

2. Umar, A.; Dunn, B. K.; Greenwald, P. Future directions in cancer prevention. Nat. Rev. Canc., 2012, 12, 835–848.

3. Dai, J.; Wu, X.; Ding, S.; Lou, X.; Xia, F.; Wang, S.; Hong, Y. Aggregation-induced emission photosensitizers: From molecular design to photodynamic therapy. J. Med. Chem., 2020, 63, 1996–2012.

4. Dougherty, T. J.; Gomer, C. J.; Henderson, B. W.; Jori, G.; Kessel, D.; Korbelik, M.; Moan, J.; Peng, Q. Photodynamic therapy. J. Natl. Cancer Inst., 1998, 90, 889–950.

5. Dąbrowski, J. M. Reactive oxygen species in photodynamic therapy: Mechanisms of their generation and potentiation. Adv. Inorg. Chem., 2017, 70, 898–8838.

6. Zhou, Z.; Song, J.; Nie, L.; Chen, X. Reactive oxygen species generating systems meeting challenges of photodynamic cancer therapy. Chem. Soc. Rev., 2016, 45, 6597−6626.

7. Kou, J.; Dou, D.; Yang, L. Porphyrin photosensitizers in photodynamic therapy and its applications. Oncotarget, 2017, 8, 81591−81603.

8. Wong, R. C. H.; Lo, P. C.; Ng, D. K. P. Stimuli responsive phthalocyanine-based fluorescent probes and photosensitizers. Coord. Chem. Rev., 2019, 379, 30−46.

9. Wang, D.; Su, H.; Kwok, R. T. K.; Shan, G.; Leung, A. C. S.; Lee, M. M. S.; Sung, H. H. Y.; Williams, I. D.; Lam, J. W. Y.; Tang, B. Z. Facile synthesis of red/NIR AIE luminogens with simple structures, bright emissions, and high photostabilities, and their applications for specific imaging of lipid droplets and image-guided photodynamic therapy. Adv. Funct. Mater., 2017, 27, 1704039.

10. Zhang, W.; Huang, Y.; Chen, Y.; Zhao, E.; Hong, Y.; Chen, S.; Lam, J. W. Y.; Chen, Y.; Hou, J.; Tang, B. Z. Amphiphilic tetraphenylethene-based pyridinium salt for selective cell-membrane imaging and room-light-induced special reactive oxygen species generation. ACS Appl. Mater. Interfaces, 2019, 11, 10567−10577.

11. He, X.; Situ, B.; Gao, M.; Guan, S.; He, B.; Ge, X.; Li, S.; Tao, M.; Zou, H.; Tang, B. Z.; Zheng, L. Stereotactic photodynamic therapy using a two-photon AIE photosensitizer. Small, 2019, 15, 1905080.

12. Li, X.; Zheng, B. D.; Peng, X. H.; Li, S. Z.; Ying, J. W.; Zhao, Y.; Huang, J. D.; Yoon, J. Phthalocyanines as medicinal photosensitizers: Developments in the last five years. Coord. Chem. Rev., 2019, 379, 147−160.

13. Liu, Z.; Zou, H.; Zhao, Z.; Zhang, P.; Shan, G.; Kwok, R. T. K.; Lam, J. W. Y.; Zheng, L.; Tang, B. Z. Tuning organelle specificity and photodynamic therapy efficiency by molecular function design. ACS Nano, 2019, 13, 11283−11293.

14. Luo, J.; Xie, Z.; Lam, J.W.Y.; Cheng, L.; Chen, H.; Qiu, C.; Kwok, H.S.; Zhan, H.; Liu, Y.; Zhu, D.; Tang, B.Z. Aggregation-induced emission of 1-methyl-1,2,3,4,5-pentaphenylsilole. Chem. Commun. 2001, 18, 1740−1741.

15. Mei, J.; Leung, N.L.C.; Kwok, R.T.K.; Lam, J.W.Y.; Tang, B.Z. Aggregation-Induced Emission: Together We Shine, United We Soar! Chem. Rev. 2015, 115, 11718–11940, doi:10.1021/acs.chemrev.5b00263.

16. Zhao, Z.; Zhang, H.; Lam, J.W.Y.; Tang, B.Z. Aggregation-Induced Emission: New Vistas at the Aggregate Level. Angew. Chem. Int. Ed. 2020, 59, 9888–9907, doi:10.1002/anie.201916729.

17. Zhou, T.; Hu, R.; Wang, L.; Qiu, Y.; Zhang, G.; Deng, Q.; Zhang, H.; Yin, P.; Situ, B.; Zhan, C.; et al. An AIE-active conjugated polymer with high ROS-generation ability and biocompatibility for efficient photodynamic therapy of bacterial infections. Angew. Chem. Int. Ed. 2020, 59, 9952–9956.

18. Ding, D.; Li, K.; Liu, B.; Tang, B.Z. Bioprobes Based on AIE Fluorogens. Acc. Chem. Res. 2013, 46, 2441–2453, doi:10.1021/ar3003464.

19. Chen, J.; Law, C.C.W.; Lam, J.W.Y.; Dong, Y.; Lo, S.M.F.; Williams, I.D.; Zhu, D.; Tang, B.Z. Synthesis, Light Emission, Nanoaggregation, and Restricted Intramolecular Rotation of 1,1-Substituted 2,3,4,5-Tetraphenylsiloles. Chem. Mater. 2003, 15, 1535–1546, doi:10.1021/cm021715z.

20. Hong, Y.; Lam, J.W.Y.; Tang, B.Z. Aggregation-induced emission: Phenomenon, mechanism and applications. Chem. Commun. 2009, 1, 4332−4353.

21. Hong, Y.; Lam, J.W.Y.; Tang, B.Z. Aggregation-induced emission. Chem. Soc. Rev. 2011, 40, 5361–5388, doi:10.1039/c1cs15113d.

22. Mei, J.; Hong, Y.; Lam, J.W.Y.; Qin, A.-J.; Tang, Y.; Tang, B.Z. Aggregation-Induced Emission: The Whole Is More Brilliant than the Parts. Adv. Mater. 2014, 26, 5429–5479, doi:10.1002/adma.201401356.

23. Nishiuchi, T.; Tanaka, K.; Kuwatani, Y.; Sung, J.; Nishinaga, T.; Kim, D.; Iyoda, M. Solvent-induced crystalline-state emission and multichromism of a bent π-surface system composed of dibenzocyclooctatetraene units. Chem. Eur. J. 2013, 19, 4110−4116.

24. Yuan, C.; Saito, S.; Camacho, C.; Kowalczyk, T.; Irle, S.; Yamaguchi, S. Hybridization of a flexible cyclooctatetraene core and rigid aceneimide wings for multi-luminescent flapping π systems. Chem. Eur. J. 2014, 20, 2193−2200.

25. Yuan, C.X.; Tao, X.T.; Ren, Y.; Li, Y.; Yang, J.X.; Yu, W.T.; Wang, L.; Jiang, M.H. Synthesis, structure, and aggregation-induced emission of a novel lambda (Λ)-shaped pyridinium salt based on Tröger's base. J. Phys. Chem. C 2007, 111, 1

2811−12816.

26. Tang, B.Z.; Kwok, R.T.K.; Li, X.; Gui, C.; Lam, J.W.Y.; Qu, J.; Tang, B.Z. A simple mitochondrial targeting AIEgen for im-age-guided two-photon excited photodynamic therapy. J. Mater. Chem. B 2018, 6, 2557–2565, doi:10.1039/c7tb02609a.

27. Tada, D.B.; Baptista, M.D.S. Photosensitizing nanoparticles and the modulation of ROS generation. Front. Chem. 2015, 3, 33, doi:10.3389/fchem.2015.00033.

28. Zhang, R.; Duan, Y.; Liu, B. Recent advances of AIE dots in NIR imaging and phototherapy. Nanoscale 2019, 11, 19241–19250, doi:10.1039/c9nr06012j.

29. Foote, C.S. Definition of TYPE I and Type II photosensitized oxidation. Photochem. Photobiol. 1991, 54, 659, doi:10.1111/j.1751-1097.1991.tb02071.x.

30. DeRosa, M.C.; Crutchley, R.J. Photosensitized singlet oxygen and its applications. Coordin. Chem. Rev. 2002, 233, 351–371.

31. Boyer, R.F.; McCleary, C.J. Superoxide ion as a primary reductant in ascorbate-mediated ferritin iron release. Free Radic. Biol. Med. 1987, 3, 389–395.

32. Gutteridge, J.M.C.; Maidt, L.; Poyer, L. Superoxide dismutase and Fenton chemistry. Reaction of ferric-EDTA complex and ferric-bipyridyl complex with hydrogen peroxide without the apparent formation of iron(II). Biochem. J. 1990, 269, 169–174, doi:10.1042/bj2690169.

33. Oszajca, M.; Brindell, M.; Orzeł, Łukasz; Dąbrowski, J.M.; Śpiewak, K.; Łabuz, P.; Pacia, M.; Stochel-Gaudyn, A.; Macyk, W.; Van Eldik, R.; et al. Mechanistic studies on versatile metal-assisted hydrogen peroxide activation processes for biomedical and environmental incentives. Coord. Chem. Rev. 2016, 327–328, 143–165, doi:10.1016/j.ccr.2016.05.013.

34. Silva, E.F.F.; Serpa, C.; Dąbrowski, J.M.; Monteiro, C.J.P.; Formosinho, S.J.; Stochel, G.; Urbanska, K.; Simoes, S.; Pereira, M.M.; Arnaut, L.G. Mechanisms of Singlet-Oxygen and Superoxide-Ion Generation by Porphyrins and Bacteriochlorins and their Implications in Photodynamic Therapy. Chem. Eur. J. 2010, 16, 9273–9286, doi:10.1002/chem.201000111.

35. Kehrer, J.P. The Haber–Weiss reaction and mechanisms of toxicity. Toxicology 2000, 149, 43–50, doi:10.1016/s0300-483x(00)00231-6.

36. Arnaut, L.G.; Pereira, M.M.; Dąbrowski, J.M.; Silva, E.F.F.; Schaberle, F.A.; Abreu, A.R.; Rocha, L.B.; Barsan, M.M.; Urbańska, K.; Stochel, G.; et al. Photodynamic Therapy Efficacy Enhanced by Dynamics: The Role of Charge Transfer and Photostability in the Selection of Photosensitizers. Chem. A Eur. J. 2014, 20, 5346–5357, doi:10.1002/chem.201304202.

37. Krzykawska-Serda, M.; Dąbrowski, J.M.; Arnaut, L.G.; Szczygieł, M.; Urbanska, K.; Stochel, G.; Elas, M. The role of strong hypoxia in tumors after treatment in the outcome of bacteriochlorin-based photodynamic therapy. Free. Radic. Biol. Med. 2014, 73, 239–251, doi:10.1016/j.freeradbiomed.2014.05.003.

38. Saavedra, R.; Rocha, L.B.; Dąbrowski, J.M.; Arnaut, L.G. Modulation of Biodistribution, Pharmacokinetics, and Photosensitivity with the Delivery Vehicle of a Bacteriochlorin Photosensitizer for Photodynamic Therapy. ChemMedChem 2013, 9, 390–398, doi:10.1002/cmdc.201300449.

39. Wilkinson, F.; Abdel-Shafi, A.A. Mechanism of Quenching of Triplet States by Oxygen: Biphenyl Derivatives in Acetonitrile. J. Phys. Chem. A 1997, 101, 5509–5516, doi:10.1021/jp970706o.

40. Schweitzer, C.; Schmidt, R. Physical Mechanisms of Generation and Deactivation of Singlet Oxygen. Chem. Rev. 2003, 103, 1685–1758, doi:10.1021/cr010371d.

41. Guan, Y.; Lu, H.; Li, W.; Zheng, Y.; Jiang, Z.; Zou, J.; Gao, H. Near-Infrared Triggered Upconversion Polymeric Nanoparticles Based on Aggregation-Induced Emission and Mitochondria Targeting for Photodynamic Cancer Therapy. ACS Appl. Mater. Interfaces 2017, 9, 26731–26739, doi:10.1021/acsami.7b07768.

42. Liu, X.; Yang, Z.; Xu, W.; Chu, Y.; Yang, J.; Yan, Y.; Hu, Y.; Wang, Y.; Hua, J. Fine tuning of pyridinium-functionalized diben-zo[a,c]phenazine near-infrared AIE fluorescent biosensors for the detection of lipopolysaccharide, bacterial imaging and photodynamic antibacterial therapy. J. Mater. Chem. C 2019, 7, 12509–12517, doi:10.1039/c9tc04427b.

43. Gao, F.; Wu, J.; Gao, H.; Hu, X.; Liu, L.; Midgley, A.C.; Liu, Q.; Sun, Z.; Liu, Y.; Ding, D.; et al. Hypoxia-tropic nanozymes as oxygen generators for tumor-favoring theranostics. Biomaterials 2020, 230, 119635, doi:10.1016/j.biomaterials.2019.119635.

44. Zhuang, Z.; Dai, J.; Yu, M.; Li, J.; Shen, P.; Hu, R.; Lou, X.; Zhao, Z.; Tang, B.Z. Type I photosensitizers based on phosphindole oxide for photodynamic therapy: Apoptosis and autophagy induced by endoplasmic reticulum stress. Chem. Sci. 2020, 11, 3405–3417, doi:10.1039/d0sc00785d.

45. Hu, F.; Xu, S.; Liu, B. Photosensitizers with Aggregation-Induced Emission: Materials and Biomedical Applications. Adv. Mater. 2018, 30, e1801350, doi:10.1002/adma.201801350.

46. Xu, S.; Duan, Y.; Liu, B. Precise Molecular Design for High-Performance Luminogens with Aggregation-Induced Emission. Adv. Mater. 2020, 32, e1903530, doi:10.1002/adma.201903530.

47. Qin, W.; Ding, D.; Liu, J.; Yuan, W.Z.; Hu, Y.; Liu, B.; Tang, B.Z. Biocompatible Nanoparticles with Aggregation-Induced Emission Characteristics as Far-Red/Near-Infrared Fluorescent Bioprobes for In Vitro and In Vivo Imaging Applications. Adv. Funct. Mater. 2012, 22, 771–779, doi:10.1002/adfm.201102191.

48. Nicol, A.; Qin, W.; Kwok, R.T.K.; Burkhartsmeyer, J.M.; Zhu, Z.; Su, H.; Luo, W.; Lam, J.W.Y.; Qian, J.; Wong, K.S.; et al. Func-tionalized AIE nanoparticles with efficient deep-red emission, mitochondrial specificity, cancer cell selectivity and multiphoton susceptibility. Chem. Sci. 2017, 8, 4634–4643, doi:10.1039/c7sc00908a.

49. Wu, W.; Mao, D.; Hu, F.; Xu, S.; Chen, C.; Zhang, C.-J.; Cheng, X.; Yuan, Y.; Ding, D.; Kong, D.; et al. A Highly Efficient and Photostable Photosensitizer with Near-Infrared Aggregation-Induced Emission for Image-Guided Photodynamic Anticancer Therapy. Adv. Mater. 2017, 29, 1700548, doi:10.1002/adma.201700548.

50. Wang, S.; Wu, W.; Manghnani, P.; Xu, S.; Wang, Y.; Goh, C.C.; Ng, L.G.; Liu, B. Polymerization-Enhanced Two-Photon Pho-tosensitization for Precise Photodynamic Therapy. ACS Nano 2019, 13, 3095–3105, doi:10.1021/acsnano.8b08398.

51. Kang, M.; Kwok, R.T.K.; Wang, J.; Zhang, H.; Lam, J.W.Y.; Li, Y.; Zhang, P.; Zou, H.; Gu, X.; Li, F.; et al. A multifunctional luminogen with aggregation-induced emission characteristics for selective imaging and photodynamic killing of both cancer cells and Gram-positive bacteria. J. Mater. Chem. B 2018, 6, 3894–3903, doi:10.1039/c8tb00572a.

52. Chen, Y.; Ai, W.; Guo, X.; Li, Y.; Ma, Y.; Chen, L.; Zhang, H.; Wang, T.; Zhang, X.; Wang, Z. Mitochondria-Targeted Poly do-pamine Nanocomposite with AIE Photosensitizer for Image-Guided Photodynamic and Photothermal Tumor Ablation. Small 2019, 15, e1902352, doi:10.1002/smll.201902352.

53. Wang, Y.; Shi, L.; Ma, D.; Xu, S.; Wu, W.; Xu, L.; Panahandeh-Fard, M.; Zhu, X.; Wang, B.; Liu, B. Tumor-Activated and Metal–Organic Framework Assisted Self-Assembly of Organic Photosensitizers. ACS Nano 2020, 14, 13056–13068, doi:10.1021/acsnano.0c04518.

54. Wan, Q.; Zhang, R.; Zhuang, Z.; Li, Y.; Huang, Y.; Wang, Z.; Zhang, W.; Hou, J.; Tang, B.Z. Molecular Engineering to Boost AIE-Active Free Radical Photogenerators and Enable High-Performance Photodynamic Therapy under Hypoxia. Adv. Funct. Mater. 2020, 30, 2002057, doi:10.1002/adfm.202002057.

55. Zhuang, W.; Yang, L.; Ma, B.; Kong, Q.; Li, G.; Wang, Y.; Tang, B.Z. Multifunctional Two-Photon AIE Luminogens for Highly Mitochondria-Specific Bioimaging and Efficient Photodynamic Therapy. ACS Appl. Mater. Interfaces 2019, 11, 20715–20724, doi:10.1021/acsami.9b04813.

56. Huang, J.; He, B.; Zhang, Z.; Li, Y.; Kang, M.; Wang, Y.; Li, K.; Wang, D.; Tang, B.Z. Aggregation-Induced Emission Luminogens Married to 2D Black Phosphorus Nanosheets for Highly Efficient Multimodal Theranostics. Adv. Mater. 2020, 32, 2003382, doi:10.1002/adma.202003382.

57. He, X.; Yang, Y.; Guo, Y.; Lu, S.; Du, Y.; Li, J.-J.; Zhang, X.; Leung, N.L.C.; Zhao, Z.; Niu, G.; et al. Phage-Guided Targeting, Discriminative Imaging, and Synergistic Killing of Bacteria by AIE Bioconjugates. J. Am. Chem. Soc. 2020, 142, 3959–3969, doi:10.1021/jacs.9b12936.

58. Shi, X.; Sung, S.H.P.; Chau, J.H.C.; Li, Y.; Liu, Z.; Kwok, R.T.K.; Liu, J.; Xiao, P.; Zhang, J.; Liu, B.; et al. Killing G(+) or G(−) Bacteria? The Important Role of Molecular Charge in AIE-Active Photosensitizers. Small Methods 2020, 4, 2000046, doi:10.1002/smtd.202000046.

59. Zhang, L.; Li, Y.; Che, W.; Li, D.; Li, G.; Xie, Z.; Song, N.; Liu, S.; Tang, B.Z.; Liu, X.; et al. AIE Multinuclear Ir(III) Complexes for Biocompatible Organic Nanoparticles with Highly Enhanced Photodynamic Performance. Adv. Sci. 2019, 6, 1802050, doi:10.1002/advs.201802050.

60. Gao, Y.; Wang, X.; He, X.; He, Z.; Yang, X.; Tian, S.; Meng, F.; Ding, D.; Luo, L.; Tang, B.Z. A Dual-Functional Photosensitizer for Ultraefficient Photodynamic Therapy and Synchronous Anticancer Efficacy Monitoring. Adv. Funct. Mater. 2019, 29, 1902673, doi:10.1002/adfm.201902673.

61. Li, Q.; Li, Y.; Min, T.; Gong, J.; Du, L.; Phillips, D.L.; Liu, J.; Lam, J.W.Y.; Sung, H.H.Y.; Williams, I.D.; et al. Time-Dependent Photodynamic Therapy for Multiple Targets: A Highly Efficient AIE-Active Photosensitizer for Selective Bacterial Elimination and Cancer Cell Ablation. Angew. Chem. Int. Ed. 2020, 59, 9470–9477, doi:10.1002/anie.201909706.

62. Zhang, P.; Kuang, H.; Xu, Y.; Shi, L.; Cao, W.; Zhu, K.; Xu, L.; Ma, J. Rational design of a high-performance quinoxalinone-based AIE photosensitizer for image-guided photodynamic therapy. ACS Appl. Mater. Interfaces 2020, 12, 42551−42557.

63. Gao, Y.; Zheng, Q.C.; Xu, S.; Yuan, Y.; Cheng, X.; Jiang, S.; Kenry; Yu, Q.; Song, Z.; Liu, B.; et al. Theranostic Nanodots with Aggregation-Induced Emission Characteristic for Targeted and Image-Guided Photodynamic Therapy of Hepatoc

ellular Carcinoma. Theranostics 2019, 9, 1264–1279, doi:10.7150/thno.29101.

64. Meng, Z.; Zhenyuan, M.; Han, G.; Liu, M.; Shan, B.; Dong, G.; Miao, Z.; Jianzhong, Y.; Tan, Z.; Li, B.; et al. Chlorin p6-Based Water-Soluble Amino Acid Derivatives as Potent Photosensitizers for Photodynamic Therapy. J. Med. Chem. 2016, 59, 4999–5010, doi:10.1021/acs.jmedchem.6b00352.

65. Xu, Y.; He, R.; Lin, D.; Ji, M.; Chen, J. Laser beam controlled drug release from Ce6–gold nanorod composites in living cells: A FLIM study. Nanoscale 2015, 7, 2433–2441, doi:10.1039/c4nr05574h.

66. Liu, S.; Li, Y.; Kwok, R.T.K.; Lam, J.W.Y.; Tang, B.Z. Structural and process controls of AIEgens for NIR-II theranostics. Chem. Sci. 2020, doi:10.1039/d0sc02911d.

67. Li, Y.; Cai, Z.; Liu, S.; Zhang, H.; Wong, S.T.H.; Lam, J.W.Y.; Kwok, R.T.K.; Qian, J.; Tang, B.Z. Design of AIEgens for near-infrared IIb imaging through structural modulation at molecular and morphological levels. Nat. Commun. 2020, 11, 1–10, doi:10.1038/s41467-020-15095-1.

68. Yu, C.Y.Y.; Xu, H.; Ji, S.; Kwok, R.T.K.; Lam, J.W.Y.; Li, X.; Krishnan, S.; Ding, D.; Tang, B.Z. Mitochondrion-anchoring photo-sensitizer with aggregation-induced emission characteristics synergistically boosts the radiosensitivity of cancer cells to ionizing radiation. Adv. Mater. 2017, 29, 1606167.

69. Zheng, Z.; Zhang, T.; Liu, H.; Chen, Y.; Kwok, R.T.K.; Ma, C.; Zhang, P.; Sung, H.H.Y.; Williams, I.D.; Lam, J.W.Y.; et al. Bright Near-Infrared Aggregation-Induced Emission Luminogens with Strong Two-Photon Absorption, Excellent Organelle Speci-ficity, and Efficient Photodynamic Therapy Potential. ACS Nano 2018, 12, 8145–8159, doi:10.1021/acsnano.8b03138.

70. Jin, G.; He, R.; Liu, Q.; Lin, M.; Dong, Y.; Li, K.; Tang, B.Z.; Liu, B.; Xu, F. Near-infrared light-regulated cancer theranostic nanoplatform based on aggregation-induced emission luminogen encapsulated upconversion nanoparticles. Theranostics 2019, 9, 246–264, doi:10.7150/thno.30174.

71. Dai, J.; Li, Y.; Long, Z.; Jiang, R.; Zhuang, Z.; Wang, Z.; Zhao, Z.; Lou, X.; Xia, F.; Tang, B.Z. Efficient Near-Infrared Photosen-sitizer with Aggregation-Induced Emission for Imaging-Guided Photodynamic Therapy in Multiple Xenograft Tumor Models. ACS Nano 2020, 14, 854–866, doi:10.1021/acsnano.9b07972.